RSC Advances

ROYAL SOCIETY OF CHEMISTRY

www.rsc.org/advances

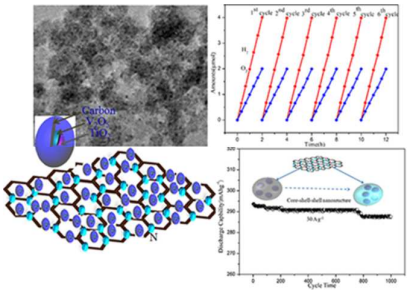

The fabricated GN-TV-C core-shell nanostructures are an alternative candidate for both energy store and photocatalysis applications.

Rational design of TiO_2-V_2O_5–C nanostructure grafted by N-doped graphene with enhanced photocatalysis and lithium ion store performances

Guohui Qin[*,ab], Xuan Wu [a,b], Hongjuan Zhang [a,b]

[a] *School of chemical Engineering & technology, Tianjin University, Tianjin 300072 , China.*

b Synergetic Innovation Center of Chemical Science and Engineering, Tianjin 300072,China.

Corresponding author:

Corresponding author. Tel./fax: +86 22 27890481.

E-mail address: guohuiq163@sina.com (G.H.Qin)

Highly ordered mesoporous crystalline C-TiO_2-V_2O_5 core-shell microspheres encapsulated by porous carbon further embedding in N-doped graphene network (GN-TV-C) nanostructures were fabricated by a simple combination of hydrothermal-calculation method. Such material exhibits a high efficiency of photocatalytic activity for water splitting as well as a high specific capacity and exceptional cycle ability in LIBs. The extrusive features of such material are the assembly of the components in a manner so as to achieve an effective integration between the constituents and the ability to modify the electronic properties of the GN-TV-C. The positive synergistic incorporation between TiO_2 and V_2O_5, the high electrical conductivity, and the three-dimensional hierarchically mesoporous nanostructure of these composites result in greatly active photocatalytic ability in patterns of increased light harvest ability and promoted exciton dissociation, excellent electrochemical performance in terms of a high rate capability, and stable cycling.

Profiting from the dual insurance from flexible carbon layer deriving from glucose and elastic GN walls with superior specific surface area, significant enhancement in electron transfer and electronic diffusion channels, highly enhanced structural stability of the TiO_2 based electrode material were simultaneously achieved. In addition, the synergistic function between TiO_2,V_2O_5 and GN involving optimized energy gap, compromised particle assemble and surface defects and its distinctive core-shell nanostructure were extensively studied. The carbon shell serves as a blocking layer to retarding the interfacial recombination in photocatalysis and protecting the active materials from pulverization during superior cycles in energy store. The current study may provide us an alternative approach in improving the performances of TiO_2 nanocrystals towards both energy store and photocatalysis applications.

Introduction

Up to present, Titanium dioxide (TiO_2) has garnered much attention given its unique nature and potential applications in a broad range of areas including environmental and energy areas from photocatalysis, solar cells, and electrochemical fields as well as lithium batteries and hydrogen generation.[1-6] In spite of its nontoxic, abundance, stability, the wide band gap of rutile TiO_2 (3.0 eV) can be excited only with UV light, which is considerably restricted when utilization of the sun light reaching the earth surface, and it still suffers from the poor lithium storage properties exhibiting limited capacity at high current rates owing to poor rate performances, which seriously hinders its large scale applications. In order to overcome the disadvantages of the TiO_2, employing doping composites to narrow its band gap and enhance its capacity

and cycle ability at the same time becomes presently urgent. Among the tremendous candidates,V_2O_5 possesses many attractive properties such as low cost, high energy density, easy synthesis, abundance as well as high theoretical capacity (~400 mA h g^{-1}) enables it be used as a pseudocapacitive anode for LIBs,[7] a wide charge storage ability because of the ability to intercalate ions in wide range of sites, and the relatively low band gap energy (about 2.3 eV) of V_2O_5, allows it to absorb over the entire solar spectrum.[8] The heterojunction of TiO_2-V_2O_5 (vanadium oxide loaded on titanium oxide surface) can serves as an effective, practical catalyst for photocatalytic applications in water splitting as well as an excellent anode material.

However, a number of unfavorable problems, such as the short lifetime of the charge carriers [9] and poor ionic and electronic conductivity, which restrict its capacity and rate capability.[10–12] To facilitate the separation and transportation of photogenerated charge carriers so as to improve the kinetics of water-splitting processes and enhance the conductivity of the electrode material in order to build blocks for preferable channels for electron and ion channels.[13–16] Several very recent studies have presented that TiO_2 based materials exposed highly-reactive facets exhibit superior photocatalytic activities as well as lithium storage capabilities.[17–21] N-doped graphene (GN) introduced in the GN-semiconductor photocatalysts has been certified to extend the visible light harvest ability, prolong the lifetime of exciton and transfer of photogenerated charge carriers and in turn improve the adsorption capacity for reactant,for which GN is pronounced to behave as an electron reservoir to capture/shuttle the electrons photogenerated from the semiconductor.[13-17] On the other

hand, GN are also observed to show stable cycle ability and excellent rate capability as anode materials in lithium ion batteries. Therefore, the heteroatom doping generates further narrow band gap of photocatalysts and the extrinsic defects interwall space for Li storage.

However, the practical application of TiO_2-V_2O_5 is restricted by the unstability of the interaction between TiO_2-V_2O_5 nanoparticles and the GN surface both for photocatalyst and anode material, it is recently reported by Zhang that the render of glucose can act as the facet-controlling agent and the connection linker by its large number of exposed hydroxyl groups.[18] The addition of glucose during the preparation of TiO_2 based materials increases the surface active sites which serves as an electron trap by capturing electrons and promotes charge separation for the photocatalytic reaction and subsequently promote the surface redox reactions and inhibits the photocorrosion problem of V_2O_5 in the photocatalysis case [19,20] and prohibits the V_2O_5 direct contact with in electrolytes, in turn, prevent its dissolution in electrolytes which can cause unfavorable side reactions, leading to rapid capacity fading during cycling in the energy store problem, which is a bottleneck problem for V_2O_5 as an anode material.

Herein, we report a simple template-free self-assembly synthesis of uniform continuous carbon layer encapsulated TiO_2/V_2O_5 mesoporous nanostructures which closely anchor on GN sheets (GN-TV-C). The intimate incorporation of TiO_2-V_2O_5 with GN is via the bulk intercalative powder between the carbon layer from glucose and GN sheets. This design possesses nanostructure engineering and combination

project with which have been demonstrated as two effective approaches for improving the TiO_2 based materials both for photocatalysts and LIBs. The visible spectrum of the as-prepared material shows extended light absorption from 400 to 600 nm. It shows remarkable photocatalytic activity for the water splitting in aqueous solution under visible light irradiation. Meanwhile, the lithium storage performance of such material was significantly enhanced in terms of excellent rate capability and superior cycle endurance. A reversible lithium storage capacity of 288.52 $mAhg^{-1}$ for up to 1000 cycles without any notable decrease can be obtained. The excellent photocatalytic and electrochemical behaviors of such complicated material are ascribed to the core-shell nature and the well-connected nanoscale heterostructure (the strong positive synergistic effect between GN and high active TiO_2/V_2O_5 nanoparticles) on the improvement of both photocatalysis and electrochemical performance. The configuration of carbon layer retards the electron-hole recombination and prevents the structural deformation upon cycling and shortens the electron-ion transfer path, while the embedded GN serves electron trapper and preserves the electrical integrity between the electrochemical active species and the current collector, which ensures the good contact between carriers with water molecule and electrode and electrolyte, respectively, in the above reaction progress.

Experimental

Material Synthesis

Graphene oxide (GO) nanosheets were firstly synthesized from natural graphite powder by a modified Hummers method.[10] The pure TiO_2 was prepared by a sol-gel

method, 3ml of $Ti(OC_4H_9)_4$ (tetrabutyl titanate, TBT) was added to 20 mL aqueous solution under vigorous mechanical stirring at 70 ℃ in water bath kept for 6 h. The milk white solution was collected by centrifuge and repeatedly washed with deionized water and acetone in turn, and then dried at 80 ℃ in static air. The observed nanocomposite was further calcinated in muffle furnace e at 800 ℃ for 5 h. V_2O_5 was coated on the TiO_2 surface by an impregnation method.[21] The prepared TiO_2 paste (1.8 g) was added in an ammonium metavanadate (NH_4VO_3,0.0690 g) solution. Subsequently, the mixture was heated at 60℃ in water bath and refluxed for 6 h. In the following procedure, the composite was dried at 120 ℃ for 8h and then annealed at 350 ℃ with a detailed heating rate of 2 ℃min^{-1} and kept in air for 4 h. Subsequently, 0.5mg of the as-synthesized white powers,150 mg glucose 133 mg urea ($CO(NH_2)_2$) were added into 67 ml GO aqueous solution. Then, the mixture was sealed in a Teflonlined stainless steel autoclave and maintained at 180 ℃ for 12 h; to prepare pure TiO_2-V_2O_5(TV) and N doped TiO_2-V_2O_5 (GN-TV) as comparison, the synthesis of GN-TV was carried out in the absence of glucose and the preparation of TV were conducted without the addition of glucose, urea and GO under the same conditions and progress as used in the synthesis of composite. Scheme 1 presents the preparation process.

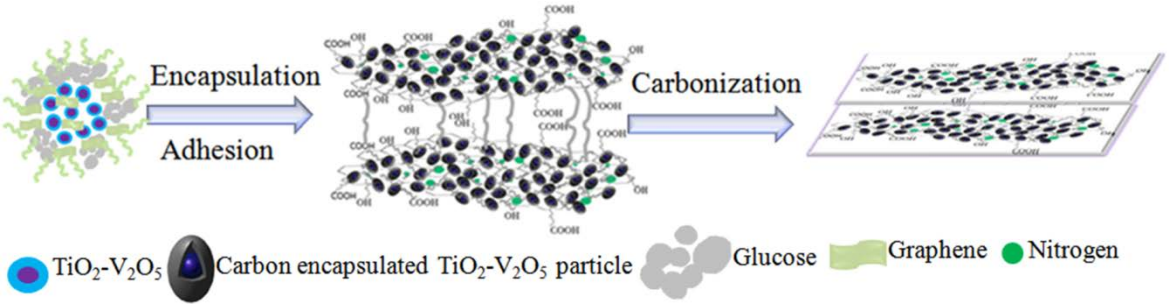

Scheme1. Schematic illustration of the synthesis procedure of GN-TV-C nanostructure

Characterization and Optics

X-ray diffraction (XRD) was performed on a Philips X'Pert Pro Super diffractometer with Cu Kα radiation (λ =1.54178 Å).The optical properties of the samples were analyzed using a UV-visible diffuse reflectance spectroscopy (DRS; V-560, JASCO).The field emission scanning electron microscopy (FE-SEM) images were taken on a JEOL JSM-6700F SEM. The transmission electron microscopy (TEM) was carried out on a JEM-2100F field emission electron microscope at an acceleration voltage of 200 kV. The high-resolution TEM (HRTEM), high-angle annular dark-field scanning transmission electron microscopy (HAADF-STEM) and corresponding energy dispersive spectroscopy (EDS) mapping analyses were performed on a JEOL JEM-ARF200F TEM/STEM with a spherical aberration corrector. X-ray photoelectron spectra (XPS) was acquired on an ESCALAB MK II with Mg Kα as the excitation source. X-ray photoelectron spectroscopy (XPS) measurements were performed using a Thermo scientific ESCA Lab250 spectrometer which consisted of monochromatic Al Kα as the X-ray source, a hemispherical analyzer and a sample stage with multi-axial adjustment to obtain the composition on the surface of samples. Raman spectra was measured using a Renishaw inVia Raman System 1000 with a 532 nm Nd: YAG excitation source at room temperature. The Brunauer-Emmett-Teller (BET) surface area was measured using a BELSORP-mini (BET Japan) at liquid nitrogen temperature (77 K).The photoluminescence (PL) spectra for the solid samples was investigated on an Edinburgh FL/FS900 spectrophotometerwith an

excitation wavelength of 360 nm. The photocurrent measurements were performed in homemade three electrode quartz cells with a PAR VMP3 Multi Potentiostat apparatus.The electrolyte was 0.2 M aqueous Na_2SO_4 solution (pH 6.8) without other additive. The electrochemical impedance spectroscopy (EIS) measurements were performed in the presence of 10mM$K_3[Fe(CN)_6]/K_4[Fe(CN)_6]$ and 0.5 M KCl by applying an AC voltage with 5 mV amplitude in a frequency range from 1 Hz to 100 kHz under open circuit potential conditions.

Photoelectrochemical measurements were carried out in a three-electrode system with a potentiostat (HSV-110,Hokuto Denko) and an electrochemical cell at room temperature. All measurements were carried out under an inert helium atmosphere and in a 1M K_2SO_4. Typically, 4 mg of catalyst and 30 μL Nafion solution (Sigma Aldrich, 5 wt %) were dispersed in 1 mL water-isopropanol solution with volume ratio of 3:1 by sonicating for 1 h to form a homogeneous ink. Then 5μL of the dispersion (containing 20 μg of catalyst) was loaded onto a FTO electrode with 3 mm diameter (loading 0.285 mg cm^{-2}). Hg/Hg_2SO_4 in 1M K_2SO_4 saturated solution were employed as the reference electrode, a Pt rod (AlfaAesar, 99.9995 %) was designed as the counter electrode, and the GN-TV-C/FTO as the working electrode, respectively. With all voltages calculated versus the reversible hydrogen electrode according to the Nernst equation:

$$V \text{ vs RHE(volt)} = V \text{ vs } Hg/Hg_2SO_4\text{(volt)} + 0.236\text{(volt)} \quad (1)$$

The Nyquist plots were measured with frequencies ranging from 1000 kHz to 1 Hz at an overpotential of 200 mV. The impedance data was fitted to a simplified Randles

circuit to extract the series and charge-transfer resistances. The irradiation wavelength was controlled by a 300 W Xe arc lamp (PLS-SXE300, Beijing Perfect light Co., Ltd.) equipped with a UV cutfilter to cut off light at wavelengths (λ>420 nm). Light intensity, as measured by a visible-irradiance meter, was about 4.0 mW/cm^2 at the position of the work electrode located. The dark currents were orders of magnitude lower than photocurrent in all cases within the voltage ranges measured.

The water splitting experiment was conducted in H-type reactor with 50 mL of 0.1M K_2SO_4 aqueous solution in each solution. A small overpotential as high as 200mV were needed to support stable H_2 and O_2 evolved rate. A bubbler purged the electrolyte in the reactor to push the evolved gases into a gas chromatograph for analysis. After that, the gas was fed back into the reactor via a recirculation pump. The gas chromatograph (SRI Instrument, Inc.) was equipped with a molecular sieve 13X packed column and a helium ionization detector. Before each reaction the system was calibrated with H_2 and O_2 gases of accurate concentration.

Electrochemical Tests

The investigation of electrochemical performance was performed by means of coin-type LIB cells (2025) assembled in an argon-filled glove box. As for anode preparation, a mixture of active material, carbon black, and polyvinylidene fluoride (PVDF) binder with a weight ratio of 80:10:10 was dispersed in Nmethylpyrrolidone (NMP) solution, and the slurry was then uniformly pasted on a Cu foil current collector. A typical electrode was dried at 120 ℃ for 24 h under v

assembled into coin cells in an argon-filled glove box. A Celgard 2400 microporous

polypropylene membrane was used as the separator and Li foil was used as the counter electrode. The nonaqueous electrolyte used was 1m $LiPF_6$ dissolved in a mixture (1:1:1,in wt%) of ethylene carbonate (EC)/dimethyl carbonate (DMC)/diethyl carbonate (DEC). Galvanostatic cycling experiments of the cells were performed on a LAND CT2001A battery test system in the voltage range of 1.00–3.00 V versus Li^+/Li at room temperature. The coin cells were activated at a current density of 0.5 C (167 mA g^{-1}) for the first cycle, and then cycled under different current densities within the voltage range of 1.00-3.00 V using a LAND-CT2001A battery test system (Jinnuo Wuhan Corp., China).Afterward, the cells were cycled under different current densities within the voltage range of 1.00-3.00 V.Electrochemical impedance spectroscopy (EIS) measurements were conducted on an electrochemical workstation (CHI 660 D, CHI Company) under a frequency range from 0.1 Hz to 100 kHz.

Results and discussions

Structure characterization

The crystal phase properties of the as-prepared TiO_2 composite were also confirmed by powder X-ray diffraction (XRD) (Fig.1a).All samples present a single-phase diffraction pattern identical to that of rutile TiO_2 (PDF#99-0090).The XRD peak position inclines to shift to lower 2q angles as the incorporation of V_2O_5, although this shift was very small evidenced by the amplified spectroscopy result (Fig S1). The crystallite size of TV could be obtained according to the Scherrer's formula $D = 0.9\lambda/\beta \cos\theta$**,** where λ is the average wavelength of the X-ray radiation, β is the line-width at half-maximum peak position, and θ is the XRD peak. The average

crystallite sizes of bulk TV and GN-TV-C sample calculated using the Scherer equation were 24 nm and 8.3 nm, respectively, indicating carbon shell and GN could induce smaller TV crystals.

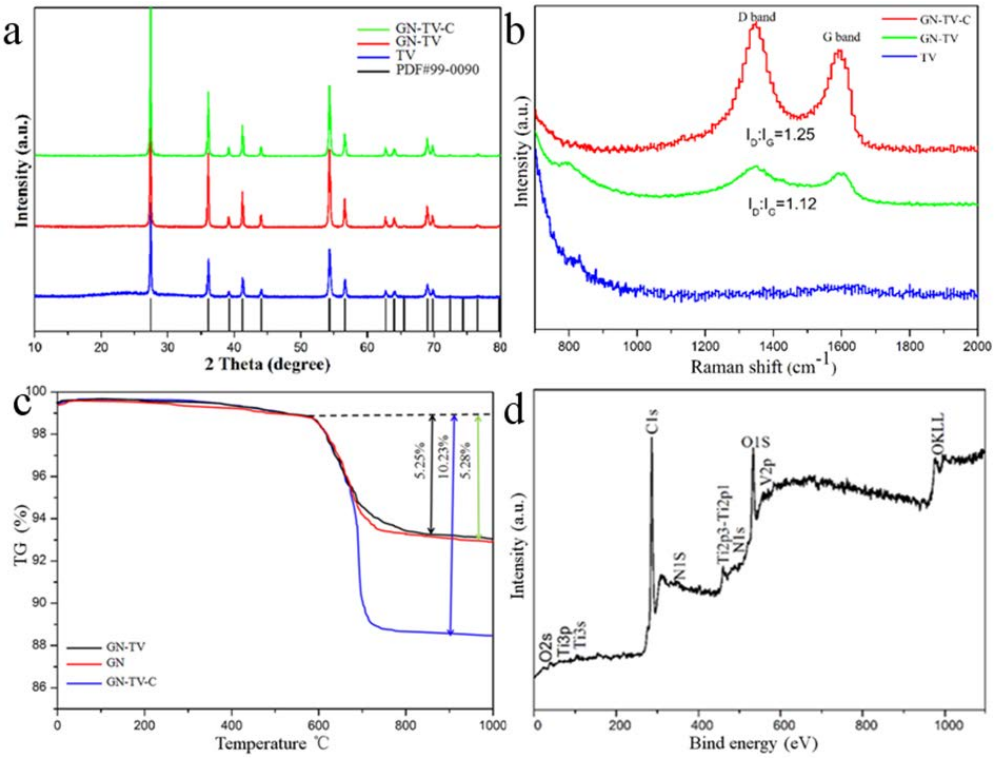

Fig.1XRD patterns of the TV samples (a) Raman spectra of the TV composites (b) TGA curves of the GN-TV-C,GN-TV and GN composites under Oxygen flow (c) and XPS survey spectrum of GN-TV-C at 700°C in NH_3 atmosphere for 1 h (d)

It appeared that the V_2O_5 component in these samples was distributed mainly near the surface, but the degree of segregation was too small to be detected by XRD, owing to the relatively low concentration of the component (V/Ti=0.01).Graphene and nitrogen were also not distinctively detected in the pattern of all the Ti samples due to their little content or amorphous feature, however, Raman shift evidences the presence of graphene in the GN-TV-C composite (Fig.1b),while the XPS spectroscopy confirms the exist of nitrogen. The two distinct peaks correspond to the

D band at ca.1350 cm^{-1} and the G band atca.1595 cm^{-1},respectively.[22] The D band is commonly ascribed to a series of structural defects, whereas the G band is observed for all graphitic structures. It is noted that the intensity ratio of the D and G bands, I_D/I_G, represents the relative concentration of sp^3 hybridized defects relatively to the sp^2 hybridized graphene domains. The average I_D/I_G values for GN-TV-C and GN-TV are 1.25 and 1.12, respectively, demonstrating that the presence of GN introduces some defects and the load of carbon layer from glucose further increase the disorder of GN-TV-C to some extent.

The carbon and nitrogen contents in the GN-TV-C composites were determined through TG analysis (Fig.1c). In the case of GN-TV, 5.25% of weight is achieved at a high temperature (800°C) due to the complete combustion of GN under air atmosphere. The TGA of GN is nearly overlapped with that of GN-TV, indicating the complete reduce of GO to graphene. The oxidative decomposition of carbon shell is believed to be ascribed to the different weight loss of GN-TV-C and GN-TV. The content of carbon shell in GN-TV-C composites can be calculated to be 4.98 %.It proves that TV composites were restricted effectively in the pores of GN-TV-C, which is consistent with the results of BET measurements as the follows (Fig S2).

N_2 adsorption/desorption isotherms were performed to study the porous feature of GN-TV-C microspheres. As shown in FigS2a, a distinct hysteresis loop between 0.8 and 1.0 was observed, which is characteristic of mesoporous materials. The pore-size distribution curve of GN-TV-C microspheres monitored by Barrett-Joyner-Halenda (t-plot) method have relatively micropores with a size distribution of 0.65–1.9 nm and a sharp peak at 30 nm (Fig S2b),demonstrating the mesoporous structure GN-TV-C

nanoparticles. The Brunauer-Emmett-Teller (BET) surface area of GN-TV-C nanostructures is calculated to be 142 m^2 g^{-1},a pore volume of 0.587 cm^3 g^{-1}, which is a significant improvement as compared with that of bulk TV nanoparticle (35 m^2g^{-1} and 0.139 cm^3g^{-1}) and the GN-TV nanocrystals (102 m^2g^{-1} and 0.413 cm^3g^{-1}),indicating the efficient of carbon shell and GN sheets in increasing the surface area of TiO_2-based nanohybrids. The substantial increase of surface area and pore volume is mainly due to the contribution GN nanosheets with a large outer surface and the porous carbon shells derived from the carbonization of glucose with inner specific area. It is believed that the larger specific surface area of mesoporous nanostructure promotes an increase in photocatalytic and electrochemical active sites, which are beneficial to improving the photocatalytic and electrochemical performances of GN-TV-C.

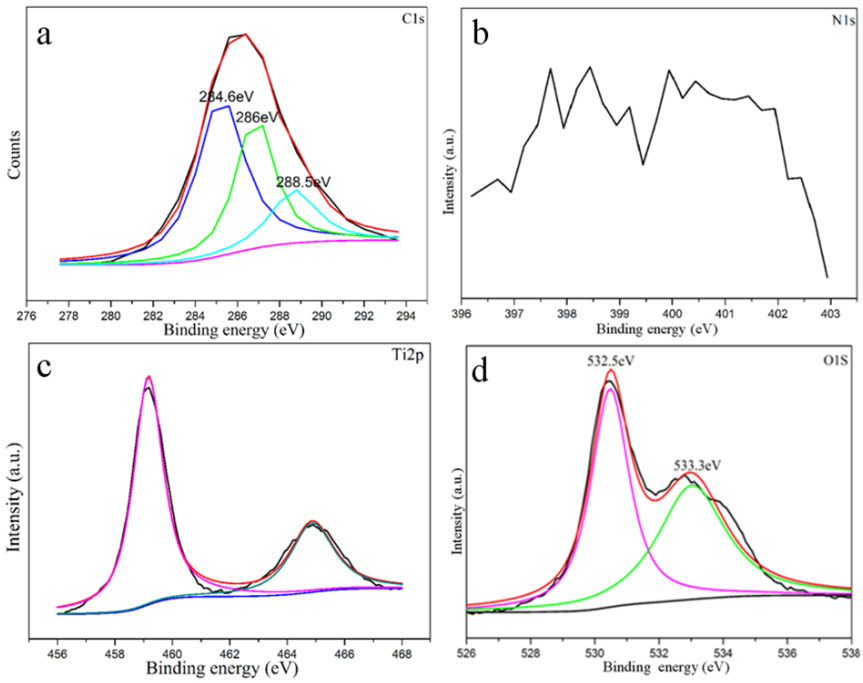

Fig.2 XPS spectrum of GN-TV-C at 700 °C in NH_3 atmosphere for 1 h:C1s narrow scan (a) N1s

narrow scan (b) Ti_{2p} narrow scan (c) O1s narrow scan (d)

Furthermore, the X-ray photoelectron spectroscopy (XPS) spectra with the total survey spectrum (Fig.1d) also verified for the existence of GN-TV-C. The C1s XPS (Fig.2a) indicates the abundance of various oxygen-containing functional groups on the graphene surface. The strong binding energy peak at 284.7 eV is assigned to the C-C bonding, 287.8 eV is assigned to the C=O bonding, and the weak binding energy peak at 289.3 eV is assigned to the O-C=O bonding, indicting the strong chemical reactivity between TiO_2-V_2O_5 and graphene, in which the TiO_2-V_2O_5 particles and GN in excellent interface binding were uniformly interconnected, which is further confirmed by SEM and TEM images of materials (Fig. 3,4 and 5).

As shown in Fig.2b, the low intensity of N1s signal implies that N is more incorporated with graphene than with TiO_2-V_2O_5.Two characteristic peaks of the Ti_{2p} spectrum at 458.2 and 463.9 eV are attributed to the $Ti_{2p3/2}$ and $Ti_{2p1/2}$ (Fig.2c), respectively.According to the relationship between the oxidation state of Ti and the separation of peak energy (Ti_{2p}), such energy gap of 5.7 eV means that the average oxidation state of elemental Ti in the GN-TV-C composite is around -3.9, showing the dominance of Ti^{4+} in the rutile TiO_2.The two peaks located at ~532.5 and ~533.3 eV attributed to the O1s (Fig.2d).In addition, for GN-TV-C core-shell-shell nanostructure, the TiO_2 core has been fully coated with the V_2O_5 shell format and continuous carbon layer deriving from glucose, the binding energy of V mainly located 517 eV and 525 eV are covered by the large amounts of O signal, thus reducing the signal intensity of the inside element and the V element is not obviously distributed in the XPS spectrum, however, V is certified in the EDS file (Fig.4).The heterojunction between core-shell-shell

TiO_2-V_2O_5/C nanostructure embedded in continuous GN network can facilitate the quick transfer of the photogenerated electrons from TiO_2-V_2O_5/C to GN. The shorten transfer time for long lived-exciton impedes the electron-hole recombination and their ability to participate in electron transfer is integral for these excitons to serve as light harvesting antennae. Besides, the flexible carbon layer and elastic GN sheets significantly improve the conductivity of the electrode material, accommodate the large volume change of GN-TV-C anode upon lithiation/delithiation, leading to an excellent cycling stability and high coulombic efficiency even at high current densities, protecting from V_2O_5 from dissolution in aqueous and electrolyte, prevent its photocorrosion under visible light irradiation and decay in long life cycle in LIBs, and thus improve the structural stability. This investigation might facilitate the high-efficient and stable hybrid photocatalysts applications in water splitting using solar energy and energy store in the development of sustainable resources. In particular, the adjustable space in the core-shell accommodates well dispersion of active nanocrystals and the retention of intact protective graphene layer finally contributes to the significantly improved cycle ability. The continuous carbon network can not only provide higher accessible surface area for the GN-TV-C nanostructures in the composite but also allow the enhanced light absorption capability and the electrolyte ions to diffuse inside rapidly, hence, it is high desirable to fabricate pore-rich materials for their potential applications in both catalysis and energy store.

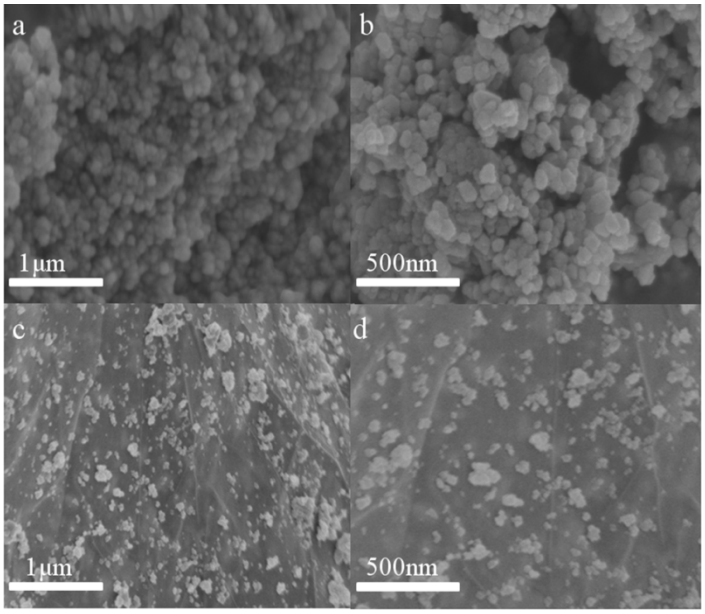

Fig.3 Images of pure TV samples at different magnifications (a) and (b) GN-TV-C composite at different magnifications (c) and (d)

The particle morphology and size of GN-TV-C samples are confirmed by SEM and TEM, as shown in Fig.3.As shown in Fig.3a and b the TV SEM images show microsized clusters with obvious agglomerated particle-like naparticles. The grain sizes are around 30nm for pure TV after annealing at 700 °C. In the case of GN-TV-C (Fig.3C), particle-like TiO_2-V_2O_5-C nanoparticles with a diameter of 20nm anchored on the GN surface with significantly decreased aggregation tendency. The uniform carbon encapsulation and the flexible GN sheets helped to prevent the agglomeration of primary crystallites of TV during calcination.

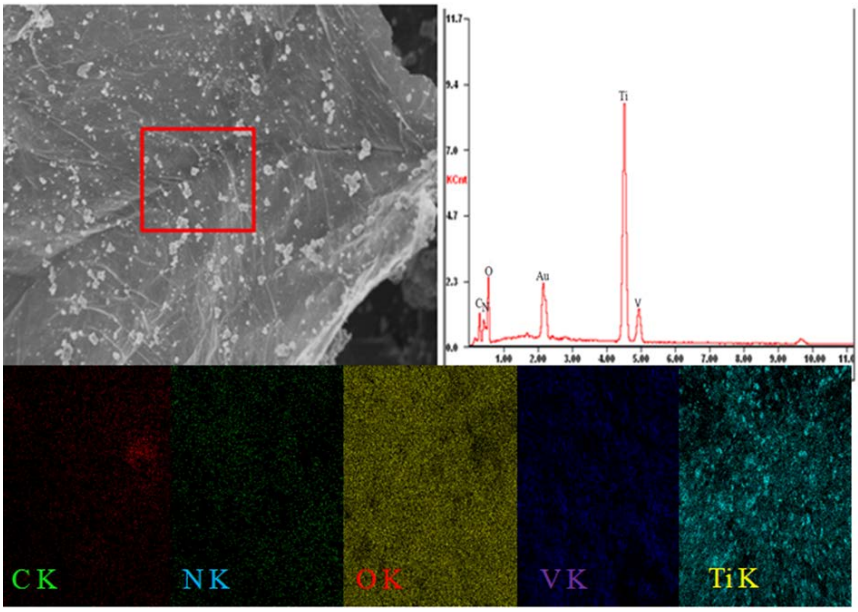

Fig. 4 EDS map of GN-TV-C nanocrystals and results of EDS analysis

To unravel the elemental composition and the amount of distribution of elements present in TV-C core/shell heterostructures, energy dispersive X-ray spectroscopy (EDS) elemental mapping was conducted. The elemental maps of this nanocomposite also suggest a uniform distribution of nitrogen, carbon ,titanium, vanadium, oxygen, which is consistent with the XRD and XPS results.

The mapping results (Fig.4) of the selected rectangular area of FESEM image of GN-TV-C clearly depicted the coexistence of T, V, O, N and C elements in the heterostructures. It is noted that the distribution of all the elements is homogeneous and uniform, but the distribution of Ti and V exhibit a much larger area than the other elements, implying that TiO_2 cores are densely and uniformly encased by V_2O_5 layer and results in core-shell-shell heterostructures.

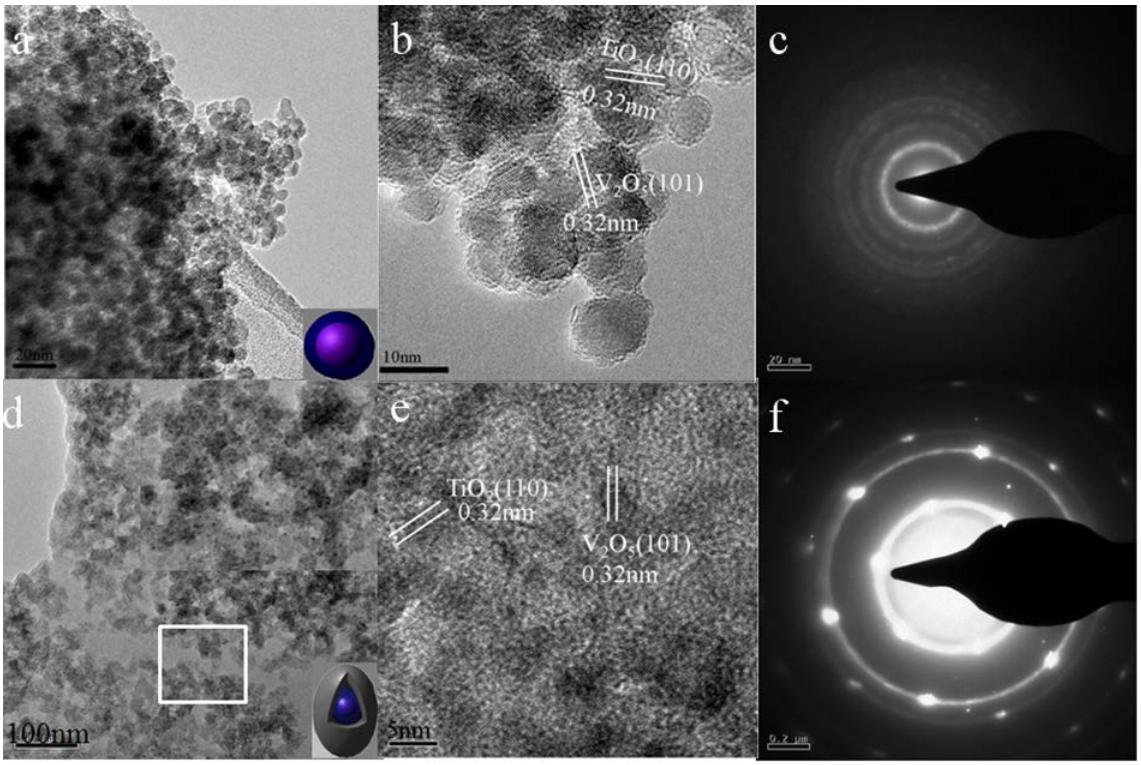

Fig.5 TEM image(A) HRTEM image (B) elected area electron diffraction (SAED) pattern for pristine TV (C) TEM image at different magnifications(D) and (E) SAED for GN-TV-C(F)

Fig.5 shows the typical TEM images of the TiO_2 samples, as shown in Fig.5a,and pure TiO_2 nanoparticles are consist of densely packed irregular nanoparticles, which is consistent with the SEM results with a high degree of crystallinity. As shown in Fig.5b, The observed HRTEM image clearly reveals the lattice spacing of 0.32 nm which corresponds to the (110) crystal planes of the rutile TiO_2 and the {101} orientation of the V_2O_5 nanoparticles, respectively. The TV nanocrystals exhibit a polycrystal of the TiO_2 (Fig.5c).

As to GN-TV-C, hardly aggregation phenomenon occurred to TV particles, which agrees with the SEM result. Meanwhile, an excessive amount of carbon led to a thick carbon-coating layer (10−20nm),TEM images in Fig.5d show the primary crystallites of TV material whose sizes ranged from 5-10 nm, TV had smaller primary crystallites

(5−10nm) than pure TV, which agrees with the XRD result. It is clear that many obvious bright regions appear in the sphere, revealing an underlying hierarchical porous structure in Fig.5d,which complies well with the result of BET. The image also shows the GN wrapping around the core shell-shell TiO_2-V_2O_5-C nanostructure.

The particles become indiscernible which were completely coated by a thick layer of carbon without respect of the high crystalline of the TV core-shell particle (read by the XRD result) (Fig.5d).There are many avoids inner the carbon layer to alleviate the volume change during the lithium-delithium progress (inset Fig.5d). This intermixing allows the TV and carbon matrix to provide especially effective mechanical reinforcement, accommodating the volume change of the active particles while also serves to separate them and inhibit their agglomeration during extended cycling. Therefore, the reinforcing GN matrix and the elastic carbon layer guarantee double insurance of the stable structure of GN-TV-C as intended. The brightness difference between the core and the shell in the magnified TEM image portrayed in the inset of Fig.5d substantiates the existence of a core/shell configuration of the heterostructures.

By analyzing the interface of the core and shell in HRTEM taken from the selected rectangular region of GN-TV-C heterostructures (as marked in Fig.5e), it is observed that the lattice fringes are continuous from core to the shell (Fig.5e). Thus, TEM and HRTEM analysis, explicitly validate the core/shell morphology of TV-C heterostructures. As clearly seen from the TEM images (Fig.5f), the polymeric morphologies were affected by thick carbon formation and the SAED in Fig.5f

showing a slightly clear six-fold pattern confirms that the crystal structure of the original graphite is retained in the exfoliated sheets and would improve by the hydrothermal reaction. This means that they are dispersed on GN sheets with good contact, the intimate contact makes the interfacial charge transfer available at the interface of the composites. Thus, Based on techniques of FESEM, FESEM,EDS elemental mapping, TEM, HRTEM and point-EDS analysis, it is safely conclude the core-shell–shell morphology of TiO_2-V_2O_5-C.

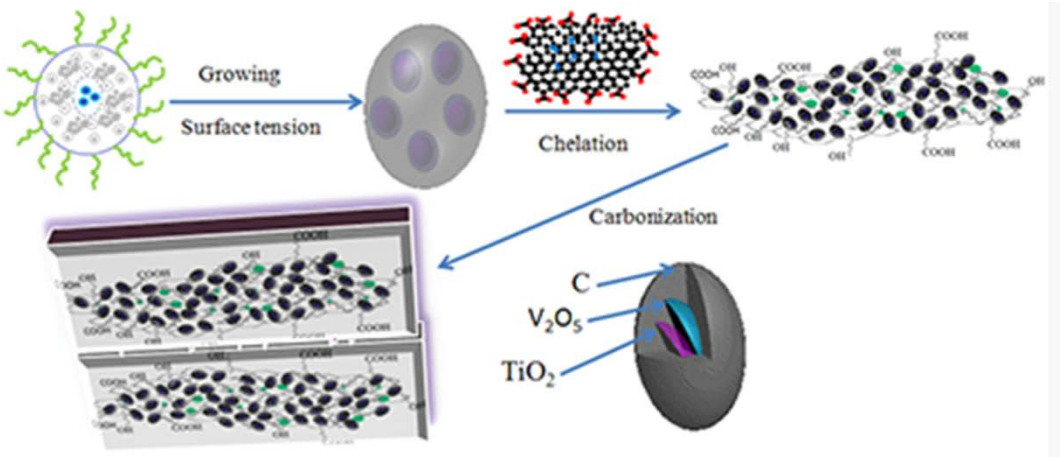

Scheme 2. Schematic illustration of the formation GN-TV-C nanostructures

The GN-TV-C crystals were concluded to form during the dissolution and recrystallization of TiO_2-V_2O_5 progress, which involved a the Ostwald ripening process.[23] As confirmed by the TEM images, the rutile TiO_2 mesocrystals were formed through the oriented self-assembly process of rutile nanocrystal subunits elongated along the {110} direction under equilibrium conditions, while the V_2O_5 finally preserves its most high active {101}. It is well concluded that {110} and {101}are the most thermodynamically stable facet for rutile TiO_2 and V_2O_5. Large amounts of oxygenated groups, hydroxyl, carbonyl and carboxyl groups can be induced on the glucose surface during the hydrothermal reation.[24] Glucose can be

expected to act as a role of surfactant,[18] in order to verify the speculation, the surface tension of the aqueous solution was investigated. Consequently, the tension reduced from 68.96 mNm^{-1} without glucose to 98.73 mNm^{-1} after the addition of glucose. Therefore, the glucose indeed predominantly play a role of surfactant during the configuration of core-shell-shell of TiO_2-V_2O_5-C, since a tension to impose on the pristine TV particles, it remains a meta-stable phase in the aqueous due to a higher surface energy the inner core, the TV nanoparticles were dissolved from inside to outside intensely enclosed by the glucose macular. The rapid dissolution and slow expansion glucose -TV led to the formation of the porous carbon shell, hence the TV particles were gradually encapsulated by the carbon microspheres since the surface tension of sphere is the lowest, and the ripening process for core-shell-shell TiO_2-V_2O_5-C micronanostructures were finished. The glucose adsorbed encapsulating the active TV with interwaving the sides of GN at the same time can be competent in face-growth inhibitors, slowing the growth of the involved face of TV and the production of mesoporous channels in the TV nanocrystals, which introduces favorable charge carrier and ion diffusion. The surface energy which is responsible for the crystallization was involved during the whole progress of the crystals growth. The TV nanostructures appear in a uniformly distributed TiO_2-V_2O_5-C morphology in the aqueous medium, whereas the nanocrystals incline to a homogeneously arranged porous core shell -shell feature. Moreover, the nanocrystal subunits were partly recrystallized during the oriented self-assembly process. The well crystalled TiO_2-V_2O_5-C densely grown on GN matrix with mesoporous nanostructure can

facilitate the quick transfer of the photogenerated electrons from TiO_2-V_2O_5-C to GN to cause the effective charge separation in the photocatalysis case as well as provide the accommodation of volume change during the charge and discharge processes in LIBs application, indicating its possible application as a visible-light driven photocatalyst and an attractive anode material candidate for LIBs. The scheme 2 illustrates the whole progress.

Optical characterization

UV−vis absorption spectras of TV,GN-TV, and GN-TV-C are shown in Fig.6a. Pure TV particles have a characteristic absorption sharp edge around 438 nm with a band-gap of 2.85 eV (Fig.6b). As for GN-TV sample, it exhibits a wider light absorption range of beyond of 489nm due to the incorporation of GN, which significantly enhance the light absorption capability due to the great surface area and its band gap calculated to be 2.75 eV. The entire absorption peak in the visible region of GN-TV-C nanocomposite shows a larger red shift (with a small band gap of 2.68 eV) compared with that of TV and GN-TV due to rational electron level, core shell-shell nanostructure, favorable surface modification of GN, its graft with V_2O_5 with narrower band gap enables its extended light harvest ability, while the core-shell nanostructure is verified to show great promise for fast separation of charge carriers and low charge recombination rate,[25] the intimate contact with GN also is also be beneficial to suppress the exciton recombination, on one hand, the highly conductive GN with great specific surface area facilitates the rapid electron separation with hole and serves as a reservoir as electrons which is convenient to the hydrogen evolution,

one the other hand, the presence of proper residual oxygen in carbon matrix (the XRD results) enhances light absorption and inhibited the recombination of charge carriers.[26] The synergistic of unique morphology and composite technique endow the GN-TV-C the dramatically enhanced photocatalysis capability, which can be expected a significant decreased charge –carrier recombination .

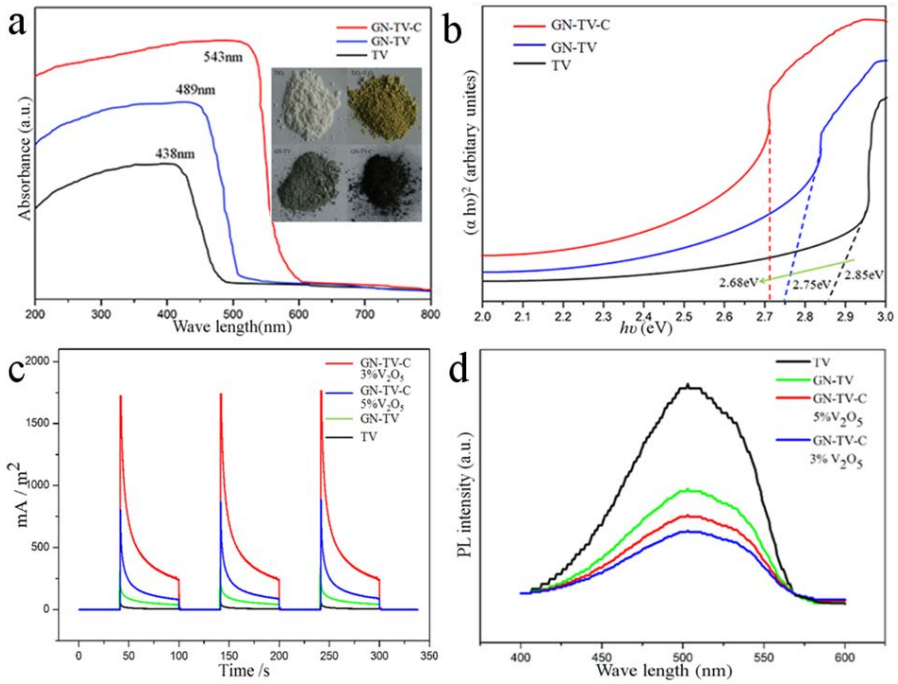

Fig. 6. The UV−vis diffuse reflectance spectra of the of the prepared TV samples (inset are the color variations of TV materials) (a) Plots of the band gap energy in direct transition recorded from the TV composite (b) Current density (mA cm^{-2}) of externally short-circuited GN-TV-C photoelectrodes under the same conditions using simulated sunlight exposure (c) and PL spectra of the TiO_2 nanoparticles (d)

The band gap energy of semiconductors can be determined based on the following formula:

$$\alpha(h\nu)=C(h\nu\text{-}Eg)^{n/2} \quad (2)$$

where α , h, v, E_g, and A are referred to absorption coefficient, Planck constant, light frequency, band gap energy, and a constant, respectively; n is 1 for direct transition

and n is 4 for indirect transition. The nature of transition is possible to be determined through plotting the graph of $(\alpha h\nu)^2$ versus $h\nu$, thereby the band gap energies can be deduced by extrapolating the straight-linear portions of the plot to intersect with the photon energy axis. Compared with TV and GN-TV, the absorption edge for GN-TV-C present an obvious blue shift, but the extend absorbance to the visible light region is mainly ascribed to the decoration of GN, this dense incorporation of GN will not only reduce the recombination efficiency of photogenerated electron–holes and improve the photocatalytic performance, but also has a good structural stability and prolongs the service life of the composites, i.e. the large 2D at structure of the GN sheets can significantly facilitate the optical transparency and provide more efficient contact between light and H_2O.The obvious narrowed band gap suggests the electronic interaction between individual components in TiO_2 and V_2O_5, which, together with the enhanced visible light absorption, could contribute to the formation and transfer of photogenerated charge transfer carriers across the interface, which is consistent with the photocurrent result of the following result.

To further investigate the characteristics of GN-TV-C arrays, photoelectrochemical measurements were performed in a three electrode. Fig.6c presents the time courses for the photocurrent of TV based materials under visible light irradiation at +0.2 V (vs. Hg/Hg_2SO_4). Obviously, the current abruptly increases and decreases as modulating the light source on and off. The incorporation of GN in the TV supply enhanced photocurrent under visible-light irradiation, the core-shell-shell configuration of TiO_2-V_2O_5-C due to the addition of glucose was

most effective for improving the visible photoresponse. It is noted that that co-doping GN and carbon shell substantially improve the photocurrent of the final GN-TV-C. Moreover, the photocurrent of GN-TV-C (3%V_2O_5) is higher than that of GN-TV-C (5%V_2O_5), thicker TiO_2-V_2O_5 contacting surface may become new carrier and holes recombination center.This implies that the amount and ratio of Ti and V are associated with the enhancement in photoactivity under visible light.

The result agreed well with the following PL measurement (Fig.6d).PL is a predominant parameter to weigh the charge separation property of the photocatalysts. The higher PL intensity means a high rate of electron–hole recombination,[27] in other words, the weaker intense the PL emission peak is, the more it suppress the photocatalytic activity. In comparison with pristine TV and GN-TV, obviously, GN-TV-C(3% V_2O_5) exhibits the most weak intense PL peak than others from Fig.6d, demonstrating that a minimium recombination of electron–holes in the TiO_2 based sample, leading to the improvement of photocatalytic activity, further addition of V_2O_5 up to 5% leads to increased electronhole recombination. It can be shown that hybrid TiO_2 with GN can cause a clear diminution of the PL emission, because the high conductive GN can trap photo-generated electrons through the interface to facilitate the charge separation to achieve a higher separation efficiency. Meanwhile, the accumulated holes on the surface of carbon layer participate in the oxygen evolution reaction, which guarantee the high oxygen production efficiency. This result was due to the fact that the electrons were excited from the valence band of TV to the conduction band and then transferred to high conductive GN, thereby

preventing direct recombination of electrons and holes. The mitigated exciton recombination leads to increased photocurrent.

Photocatalysis performance

Solar-driven water splitting with 250mV is achieved under visible light (>420nm) using the as-synthesized TV samples. For electrode preparation, the prepared TV was deposited on a fluorine-doped tin oxide (FTO) substrate, introducing a Pt electrode as the counterpart electrode. Fig.7a displays the evolution of H_2 and O_2 gases from the TV samples dispersed in electrolyte. The 2:1 stoichiometry between H_2 and O_2 with the linear increase of gas concentrations confirms the water-splitting photoactivity. Among the three TV samples, the GN-TV-C(3%V_2O_5) have the highest efficiency (3.987 and 1.993μmol h^{-1} for H_2 and O_2 from 2.0 mg of nanotree heterostructures per hour),while those of the other two samples just reached 2.96 and 1.43, 1.18 and 0.58μmol h^{-1}, respectively for GN-TV and TV, which agree with all the aforementioned results. GN sheet based on a rational percentage could serves as a rapid electron transport path way for high carrier separation and the electron collection at the conductive substrate. The core-shell-shell TiO_2-V_2O_5-C nanocrystals could prevent the directly contact between the exposed GN surface (rich in negatively charged electrons) and the electrolyte (rich in positively charged holes),which could substantially reduce the recombination rate of the photogenerated carriers.Such photocatalyst can endure continuous 12h working time test without obviously decreased working efficiency (Fig.7b), further certify the strongly nanostructure stability.

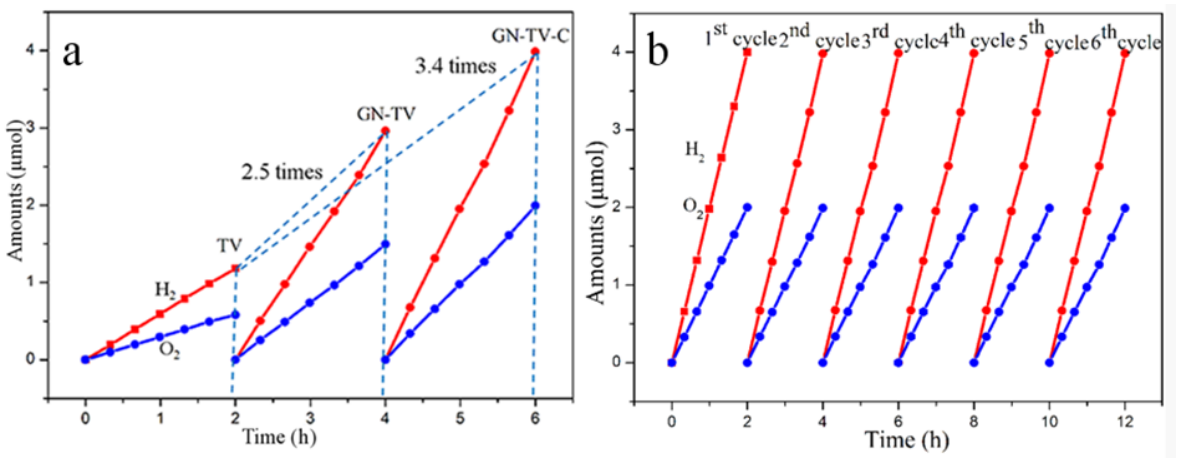

Fig.7 The evolution of H_2 and O_2 gases of TV samples (a) Stability of photocatalytic water for GN-TV-C nanocomposite under visible light irradiation (b)

The photocatalysis mechanism was shown in Fig.8. The photo-excited electrons would transfer from TV to FTO then to Pt, and the separated electrons on the surface of Pt would combine with adsorbed H^+ to produce H_2.At the same time, the accumulated holes on the surface of TV would firmly retained within the surface of carbon layer due to its positive band layer,[26]which would oxidize the H_2O to release O_2.Compared with bare TV, the GN-TV-C heterostructures had prolonged the life time of separated exciton pairs, resulting in the improvement of H_2 and O_2 production.

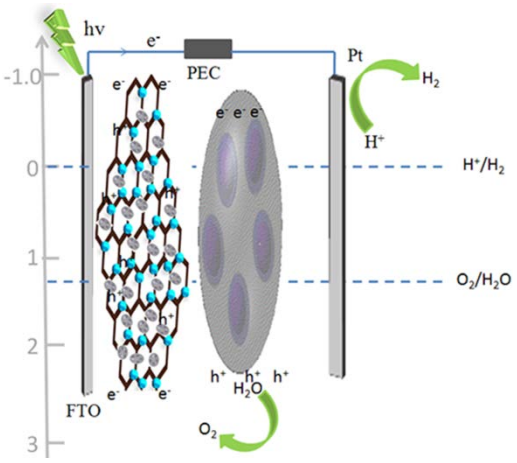

Fig. 8 The photocatalysis mechanism for GN-TV-C

Electrochemical performances

Cyclic voltammetry was conducted in order to investigate the effect of the

electrochemical properties of the TV based samples by using a scanning rate of 0.5mVs^{-1}, voltage range: 1.00–3.00V.A single pair of sharp oxidation and reduction peaks, a plateau at 2.0V and a sloped region of 1.7–1.0 V, corresponding to the typical lithiation and de-lithiation process of TiO_2, respectively, can be clearly discerned. Interestingly, V_2O_5 presents electrochemical inactive in the three samples, but is observed to contribute to capacities. Fig.9a presents the comparison of the CV profiles of pristine TV, GN-TV and GN-TV-C in the first cycle. For pristine TV, the oxidation and reduction peaks are observed at 2.21 and 1.72 V, respectively, with the polarization being 0.49 V.As to GN-TV, the oxidation and reduction peaks appears at 2.16 and 1.78 V, respectively, and the polarization is 0.38 V.As for GN-TV-C, the oxidation and reduction peaks occurs at 1.96 and 1.72 V, respectively, with the polarization just decreases to 0.24 V. Broadened peaks of pristine TV present the most poor kinetics, lithium intercalation and deintercalation is sluggish. The lower polarization and higher peak of GN-TV-C sample compared to that of TV correlate with the unique core-shell-shell nanostructure coating. Since the active TV is confined in the amorphous porous carbon shell on the nanoscale, meanwhile, keeps a intimate contact with the interwaved GN channels, the electron transfer and lithium ion diffusion paths are dramatically decreased, hence, resulting in significantly enhanced reversibility. Besides, the inertness of carbon with more exposed active cites leads to better Li kinetics, poor adsorption leads to Li clustering, significantly affecting the performance of the battery.[28]

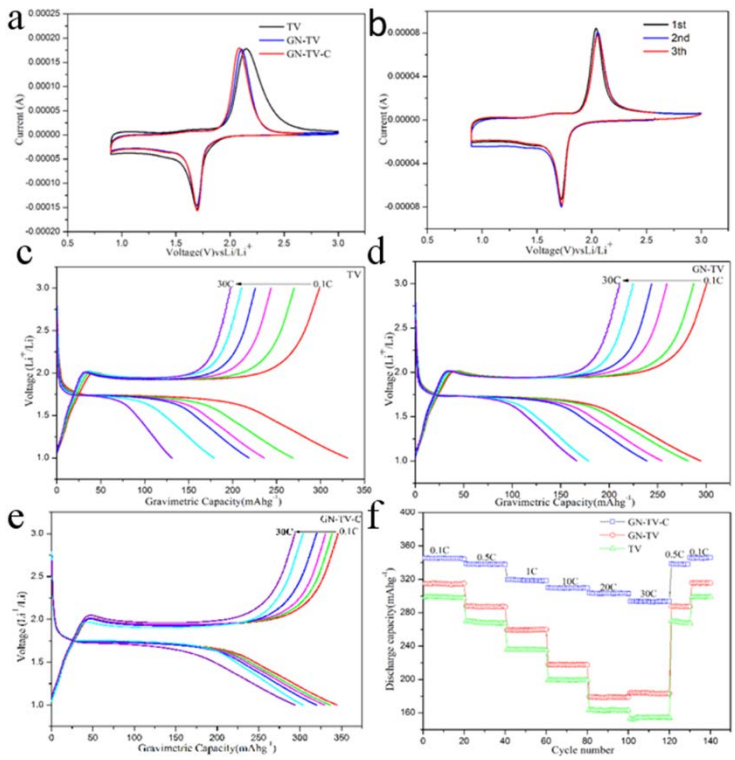

Fig.9 Cyclic voltammetry curves of all $LiFePO_4$ samples at 0.5 mVs^{-1}(a) Charge/discharge curves CV curves of the composite GN-TV-Cat a scan rate of 0.5 mV s^{-1}(b) Charge/discharge curves of TV sample (c) GN-TV composite (d) GN-TV-C (e) and The rate performance curves of TV samples (f)

Cyclic voltammograms (CV) of GN-TV-C from the 1st to 3rd cycle at a scan rate of 0.5 mV s^{-1} in the voltage range of 1.0–3.0 V is illustrated in Fig.9b.It can be observed that the intensity of the redox peaks increased during the second and third scan, implying a possible activating process in the electrode material. The second and third cycles with higher cathodic peaks and lower anodic peaks compared to the initial cycle are nearly overlapped, supporting the excellent electrochemical reactivity of modified TiO_2 composites. The plots replication certifies the good reversibility of the lithium extraction–insertion reactions in terms of small polarization, which well complies with aforementioned discussions. Fig.9 (c, d and e) describes the

galvanostatic charge discharge voltage profiles of cells for all TV samples at progressively increased C rates from 0.1 C to 30 C between 1.00 and 3.00 V vs. Li^+/Li. It is noted the voltage plateau is lengthened for the GN and C modified TV materials, which should be ascribed to the higher electrochemical reactivity of modified TV and excellent kinetics. This result is consistent with the CV profiles. The modified TV materials exhibit higher capacities than TV at a low rate C/10, and a maximum capacity of 345.59 $mAhg^{-1}$ are observed in GN-TV-C, while that of the GN-TV and TV reach 300.50, 298.58 $mAhg^{-1}$,respectively.In addition, it is found that a serious polarization tendency at high C rates, while the modified samples have a slight polarization tendency. Fig.S3 compared the charge-discharge files of 3% V_2O_5 and 5% V_2O_5,it is observed that that the capacity of later decreased obviously, too much V_2O_5 can introduce more structure instability due to the irreversible phase transitions outweight its contribution to the capacity of TV during charge-discharge progress.[29]

Fig.9f is the cycling performances at various current density from $100mAg^{-1}$ to 30 Ag^{-1}. It can clearly shown that, compared to the GN-TV and pure TV samples, the specific capacity of the GN-TV-C sample is substantially higher at all investigated charge-discharge rates. For example, the GN-TV-C electrode displays a much superior rate performance of 303.69 and 293.81 mAh g^{-1},which is 1.3 times that of the GN-TV electrode (243.79 and 238.95 mAh g^{-1}) and is almost 2 times of that for pure TV (201.41,179.26 mAh g^{-1}) at current densities of 20 and 30 Ag^{-1}, respectively. Recovering the current density back to 50 mAg^{-1} and 100 mAg^{-1}, reversible capacities of up to their initial capacities, verifying the good reversibility and structural stability

of the GN-TV-C anode composite and the capacity keeps ascending during subsequent cycling, approaching its initial capacity. The excellent rate capability arises from the 3D interconnected porous core-shell-shell carbon structure and the GN interwaved favorable channels, which not only offers multidimensional channels for the electrolyte access and sufficient void space to buffer the volume change of TV during cycling but also effectively shortens the electronic/ionic transport path. In particular, the excellent mechanical stability of the carbon layer greatly confines the active TV particles in the core shell nanostructure impeding the corrosion from electrolytes and meanwhile the good conductivity of the 3D interconnected GN matrix results in the long cycle ability of GN-TV-C. The reversible formation of flexible carbon buffering layer and elastic graphene sheets restrain the volume change of TV during the charge and discharge processes.

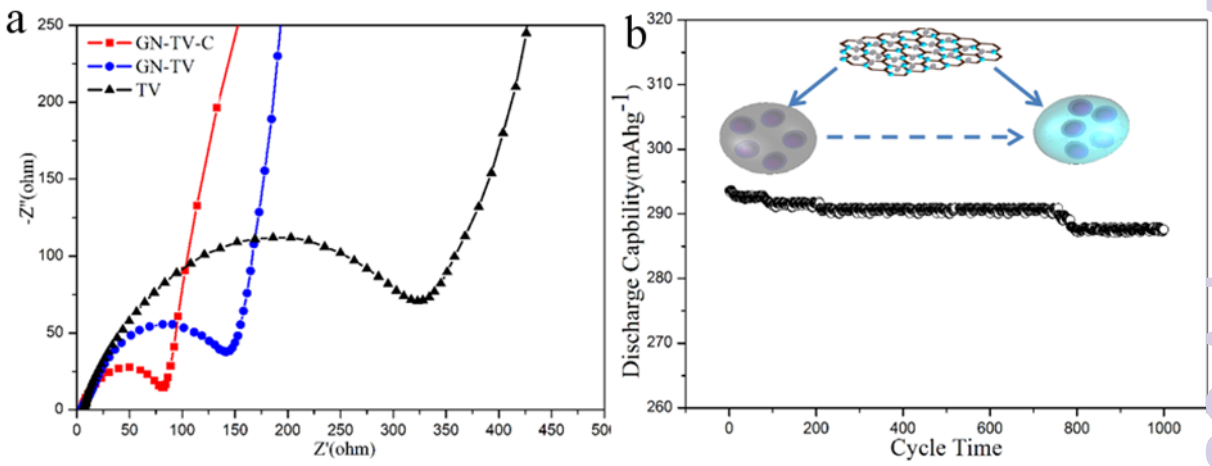

Fig.10 Electrochemical impedance spectroscopy (EIS) result of the TV samples(a) and long-term stability for GN-TV-C material 30Ag^{-1}(b)

The heterostructure GN-TV-C exhibits an excellent rate capability compared to the GN-TV and TV samples, however, the difference in conductivity between them should be taken into account. Electrochemical impedance spectroscopy (EIS)

measurements were performed to investigate the conductivity of the cathodes composed of TV based electrodes. As shown in Fig.10a,the GN-TV-C electrode possesses a much lower resistance than that of the GN-C and TV electrodes (ca. 73.2 vs. 145.9 and 330.4 Ω, respectively), implying that the encapsulation of core -shell-shell nanostructure and GN matrix can significantly enhance the electrochemical kinetics. The synergistic effect of the successful integration of the TV structure and interwaved GN matrix is beneficial to the structure stability during the photocatalysis and charge and discharge progresses. Ideal electrode materials are both good electronic and ionic conductors. The electrons and Li ions must reach or leave the reaction point simultaneously. However, for TV, it not only suffers from extremely low intrinsic electronic conductivity due to lacking of effective conductive carbon layers on its surface. Thus the larger particle size for pure TV may decrease the electronic conductivity in the bulks and result in the higher charge-transfer impedance Rct.[30]

In particular, the lower electron transfer resistance can effectively accelerate the transfer mechanism of photo-generated charges in the hetero-structured samples, positively suppressing the combination of the photo-generated electron–hole pairs and further enhances the reactive activities of these samples, which is beneficial for the enhancement of photocatalytic performance and extending the sunlight harvest ability. Therefore, the synergistic morphology and composite engineering together with the particular mesoporous nanostructure introduce a promising candidate for both photocatalysis and energy store.

The robust nanostructure of GN-TV-C was further investigated (Fig.10b), the morphology of GN-TV-C were examined after the 2000 times cycling test.Fig.S4 show that the TEM image of the core-shell structure of TiO_2-V_2O_5-C is remained escaping from pulverization after 1000 times cycling, which is attractively pursued when designing anode materials. With the dual protections from GN and carbon layer, the severe volume changes of TV can be effectively accommodated. The carbon layer can also protect the TV electrode from electrolyte corrosion and maintain the structural stability of the TV, thus resulting in much improved rate and low temperature capability and cycle stability of the GN-TV-C, which agree well with the aforementioned results.

Conclusions

In summary, coupling morphology technology and composite engineering to GN-TV-C lead to both the photocatalytic and energy store enhancements. In this project, rational combination of TiO_2 with V_2O_5 (3% V_2O_5) encapsulated by uniform carbon nanocages which is embedded in interconnected GN channels was fabricated for water splitting and lithium ion batteries. As to the forth, due to its the optimized band gap, short distance between the core and its surface, the photogenerated electrons and holes could be easy transferred to the surface for reaction, effectively extending the light harvest ability, improving the utilize efficiency of exciton and photoelectron stability. Besides, the carbon layer films that possess more amorphous regions induce more exciton production in the photocatalysis procedure, and allow for more space to effectively alleviate the volume change during lithium

insertion/extraction progress, and provide more active sites for both cases. For the later, owing to the shortened Li^+ diffusion distance, high contact surface area, good electronic conductivity, and superior structure stability of carbon-encapsulated core–shell nanostructure, high reversible rate capability and cycle ability are achieved. This simple and efficient synthetic protocol incorporation of morphology and surface modification can be further extended to build up other composited nanomaterials based on earth-abundant elements with promising applications in catalysis, sensing, supercapacitors, and lithium batteries and sodium batteries.

Acknowledgements

The authors thankfully acknowledge the support of National Science Foundation of China (No.51172160) for financial supports.

References

1T.Butburee, Y.Bai, J.Pan, X.Zong, C.H.Sun, G.Liu, L.Z.Wang,*J. Mater. Chem. A.***2014**, 2, 12776.
2 M.Q.Yang, Z.Nan,Y.J. Xu, *ACS Appl. Mater. Interfaces.* **2013**, 5, 1156.
3 G.H.Qin, X.Y.Zhang, C.Y.Wang, *J. Mater. Chem. A.* **2014**, 2, 12449.
4W.Li,F.Wang,S.Feng,J.Wang,Z.Sun,B.Li,Y.Li,J.Yang,A.A.Elzatahry,Y.Xia,D.Zhao,*J.Am.Chem.Soc.***2013**, 135, 18300.
5Q.P.Wu, J.Zhao, G.H.Qin, C.Y.Wang,X.L.Tong, S.Xue, *Appl.catal.,B.* **2013**,142, 142.
6 G.H.Qin, H.J.Zhang, C.Y.Wang, *J. Power Sources*,**2014**,272, 491.
7 J.Liu, H. Xia, D.Xue, L.Lu, *J.Am.Chem.Soc.* **2009**,131 ,12086.
8 S.L. Xie, T. Zhai, W.Li, M.H. Yu, C.L.Liang, J.Y.Gan,X.H.Lu, Y.X.Tong ,*Green Chem.* **2013**, **15**, 2434
9S. H.Choi,Y.C.Kang, *Chem. Eur. J.* 2014, 20, 1.
10Y.Qiao,X.L.Hu,Y.Liu,C.J.Chen,H.H.Xu,D.F.Hou,P.Hu,Y.H.Huang,*J.Mater.Chem.A.***2013**,1, 10375.
11 A.R.Armstrong, G.Armstrong, J.Canales, R.Garc´ıa, P. G.Bruce, *Adv. Mater.* **2005**, 17, 862.
12 J. Wang, Y.Zhou, Y.Hu, R.O'Hayre, Z. *J.* Shao, *Phys. Chem. C*. **2011**, 115, 2529.
13 B.Weng, J. Wu, N. Zhang, Y. J.Xu, *Langmuir*. DOI: 10.1021/la4048566.
14Q.Li, B.Guo, J.Yu, J.Ran, B.Zhang, H. J.Yan, J.R.Gong, *J.Am.Chem.Soc.***2011**,133,10878.
15Y.T.Liang, B.K.Vijayan, O. Lyandres, K. A.Gray, M.C.Hersam, *J.Phys.Chem.Lett.***2012**,3, 1760.
16 T.Xu, L.Zhang, H.Cheng, Y. Zhu, *Appl. Catal., B.* **2011**, 101, 382.
17 N.Zhang, Y.Zhang, M. Q.Yang, Z.R.Tang, Y. J.Xu, *J. Catal.* **2013**, 299, 210.
18 B.C.Qiu, M.Y.Xing, J.L.Zhang, *J.Am. Chem. Soc.***2014**,136, 5852.
19 S.Y.Guo, S. Han, B.Chi, J. Pu, J. Li, *ACS Appl. Mater. Interfaces.* **2014**, 6, 4743.
20 T.Hisatomi, J.Kubota, K. Domen, *Chem. Soc. Rev.* DOI: 10.1039/c3cs60378d.
21 W.Zhao, Q.Zhong, *RSC Adv.* **2014**, 4, 5653.
22 D.Wei, Y. Liu, *Adv. Mater.***2010**, 22, 3225-3241.
23 B. Li, G.Rong, Y.Xie, L.Huang, C.Feng, *Inorg. Chem.***2006**, 45, 6404.
24 G.H.Qin, Q.P. Wu, J.Zhao, Q.Q.Ma, C.Y.Wang, *J.Power Sources*. **2014**,248, 588.
25 H.Guo, W.Wang, L.Liu, Y.He, C.Li, Y. Wang, *Green chem.*, **2013**,15, 2810.
26 Li,Q.;Zhang, N.; Yang,Y.; Wang, G.Z.; Ng, D.H.L. *Langmuir.* **2014**, 30, 8965.
27 S.Usai, S.Obregón, A.I.Becerro, G. Colón, *J. Phys. Chem. C*. **2013**, 117, 24479.
28 M.Q.Yang, Y.J.Xu, *J. Phys. Chem. C.* **2013**, 117, 21724.
29 X. F.Zhang, K. X.Wang, X.Wei, J. S. Chen, *Chem. Mater.* **2011**, 23, 5290.
30M. E. Stournara, Y. Qi, V. B. Shenoy, *Nano Lett.* **2014**, 14, 2140.